Chemical Science

EDGE ARTICLE

View Article Online
View Journal | View Issue



Cite this: *Chem. Sci.*, 2017, **8**, 5650

# From single-site tantalum complexes to nanoparticles of $Ta_xN_y$ and $TaO_xN_y$ supported on silica: elucidation of synthesis chemistry by dynamic nuclear polarization surface enhanced NMR spectroscopy and X-ray absorption spectroscopy†

Janet C. Mohandas,[a] Edy Abou-Hamad,‡[a] Emmanuel Callens,‡[a] Manoja K. Samantaray,[a] David Gajan,[b] Andrei Gurinov,[a] Tao Ma,[c] Samy Ould-Chikh,[a] Adam S. Hoffman,[c] Bruce C. Gates*[c] and Jean-Marie Basset*[a]

Air-stable catalysts consisting of tantalum nitride nanoparticles represented as a mixture of $Ta_xN_y$ and $TaO_xN_y$ with diameters in the range of 0.5 to 3 nm supported on highly dehydroxylated silica were synthesized from $TaMe_5$ (Me = methyl) and dimeric $Ta_2(OMe)_{10}$ with guidance by the principles of surface organometallic chemistry (SOMC). Characterization of the supported precursors and the supported nanoparticles formed from them was carried out by IR, NMR, UV-Vis, extended X-ray absorption fine structure, and X-ray photoelectron spectroscopies complemented with XRD and high-resolution TEM, with dynamic nuclear polarization surface enhanced NMR spectroscopy being especially helpful by providing enhanced intensities of the signals of $^{1}H$, $^{13}C$, $^{29}Si$, and $^{15}N$ at their natural abundances. The characterization data provide details of the synthesis chemistry, including evidence of (a) $O_2$ insertion into $Ta-CH_3$ species on the support and (b) a binuclear to mononuclear transformation of species formed from $Ta_2(OMe)_{10}$ on the support. A catalytic test reaction, cyclooctene epoxidation, was used to probe the supported nanoparticles, with 30% $H_2O_2$ serving as the oxidant. The catalysts gave selectivities up to 98% for the epoxide at conversions as high as 99% with a 3.4 wt% loading of Ta present as $Ta_xN_y/TaO_xN_y$.

Received 27th March 2017
Accepted 8th June 2017

DOI: 10.1039/c7sc01365e

rsc.li/chemical-science



## Introduction

Dispersed species ranging from single-metal-atom complexes to clusters and nanoparticles (NPs) of metals and metal oxides are materials that find many applications, especially in catalysis.[1–3] Numerous methods have been used to synthesize such NPs, often involving colloidal, solution-based, or chemical or physical vapour-deposition techniques.[4,5] Solution-based methods often suffer from the need for capping agents or surfactants to stabilize the clusters or NPs, and deposition methods lack fine control and typically lead to highly nonhomogeneous materials.[6,7] In typical catalytic applications, NPs are dispersed on high-area porous supports such as silica, alumina, and zeolites.[8,9] The supported NPs are often unstable, undergoing agglomeration or sintering during operation.[10]

A foundation for the synthesis of NPs from molecular building blocks on supports is provided by surface organometallic chemistry. Thus, the supported species can be made without the need for templates, capping agents, or surfactants, and the syntheses thereby offer good prospects for control of the compositions and sizes of the dispersed species. Essential reactant species in such syntheses are the support surface functional groups, exemplified by the –OH groups on silica. Control of the sizes of NPs synthesized from single-metal-atom precursors on supports may be facilitated by the initial bonding of the precursor species to the support to minimize agglomeration. Thus, for instance, surface organometallic chemistry has guided the synthesis of monometallic (Pt) and bimetallic (Pt–Sn) clusters on silica, giving catalysts with high activities and selectivities for catalytic hydrogenolysis, isomerization, and dehydrogenation reactions.[11–13] However, only little work has been done to extend the concepts to non-metal NPs including

[a]*King Abdullah University of Science & Technology, KAUST Catalysis Center (KCC), 23955-6900 Thuwal, Saudi Arabia. E-mail: jeanmarie.basset@kaust.edu.sa*

[b]*Institut de Sciences Analytiques (CNRS/ENS-Lyon/UCB-Lyon 1), Université de Lyon, Centre de RMN à Très Hauts Champs, 69100, Villeurbanne, France*

[c]*Department of Chemical Engineering, University of California, Davis, California 95616, USA. E-mail: bcgates@ucdavis.edu*

† Electronic supplementary information (ESI) available: Complete experimental procedures, supporting characterization techniques, data and the details for the prepared compounds are provided. See DOI: 10.1039/c7sc01365e

‡ These authors contributed equally.

semiconductors, and herein we demonstrate their use to guide the synthesis of silica-supported metal nitride semiconductor NPs.[14] Such materials offer prospects as new catalysts, and they could also offer unique optoelectronic properties of potential value in displays, quantum computing, or photovoltaic devices.[8,15–22]

Unsupported nanocrystalline samples consisting of TaON and $Ta_3N_5$ were used by Gao *et al.*[17] to catalyze cyclooctene epoxidation, an industrially important reaction. Epoxidation reactions are sensitive to catalyst surface acidity or basicity, and by incorporating nitrogen in place of oxygen in the framework of $Ta_2O_5$, these authors tuned the catalyst basicity and improved its properties.

Syntheses of metal nitrides often lead to mixed phases or non-stoichiometric compositions. Strategies to control metal nitride synthesis have been developed, some involving the application of various nitriding agents such as gaseous or liquid $NH_3$, urea, cyanamide, *etc.*[20,22] A traditional method involving gaseous $NH_3$ is convenient for the synthesis of impurity-free metal nitrides, because the high treatment temperatures lead to the release of $N_2$ and $H_2$, which react with oxides and form water,[21,23–25] which can be removed as a gas. Hence, we reasoned that it would be of interest to attempt analogous syntheses to make dispersed metal nitrides on a support, being guided by surface organometallic chemistry and starting with molecular metal complexes anchored to the support. We chose silica as the support because its surface chemistry is well understood and the principles of surface of organometallic chemistry are a powerful guide to manipulating syntheses on it. We chose tantalum as a precursor metal to allow a comparison of our results with those of Gao *et al.* for the performance of tantalum nitride catalysts for cyclooctene epoxidation.

Understanding the chemistry of species dispersed on solid surfaces emerges best when a battery of complementary characterization techniques is applied to allow elucidation of elementary reactions. Dynamic nuclear polarization surface enhanced NMR spectroscopy (DNP SENS) is especially powerful for elucidation of dispersed surface species and their transformations. The technique requires a simple impregnation of the sample with a stable free radical such as bi-radical nitroxide (TEKPol).[26] The effective polarization transfer of free electrons of the radical to the surrounding nuclei (usually $^1H$) induced by microwave radiation and subsequent cross polarization to the nuclei of interest ($^{13}C$, $^{15}N$, $^{29}Si$, $^{17}O$, *etc.*) are essential for the success of this recently developed technique. It allows NMR measurements with signal enhancements, leading to well-resolved spectra of any nuclei of interest.[26–30]

Taking advantage of this technique, we now report two strategies for the synthesis of air-stable, supported NPs of $Ta_xN_y$ and $TaO_xN_y$ with sizes in the range of 0.5–3 nm, from well-defined molecular precursors without using any capping agents or surfactants. Such syntheses of finely sized NPs of tantalum nitride have not yet been known. The precursors, $TaMe_5$, **1**, and the dimeric $Ta(OMe)_5$, **2**, were first grafted onto silica (Aerosil $SiO_2$-700-dehydroxylated at 973 K (700 °C)). Subsequent treatments led to the formation of $Ta_xN_y/TaO_xN_y$ NPs, which were tested as catalysts for epoxidation of cyclooctene. Conventional characterization techniques were sufficient to demonstrate the formation of the NPs, but understanding of the elementary steps of the surface chemistry required the application of DNP SENS.[26–30] Further details of the surface tantalum species, including interatomic distances and coordination numbers, were obtained from extended X-ray absorption fine structure (EXAFS) spectra.[31–34]

## Results and discussion

### Summary of synthesis chemistry of silica-supported tantalum nitride nanoparticles from silica-supported tantalum complexes

To begin, we provide a summary roadmap, Scheme 1, illustrating the two synthetic strategies used to prepare the NPs referred to as $Ta_xN_y/TaO_xN_y$. These were prepared from $TaMe_5$, **1**, and $Ta(OMe)_5$, **2** (which exists as a dimer). The evidence for this chemistry is presented in the paragraphs that follow. The spectroscopic data show that **1** and **2**, upon grafting onto $SiO_2$-

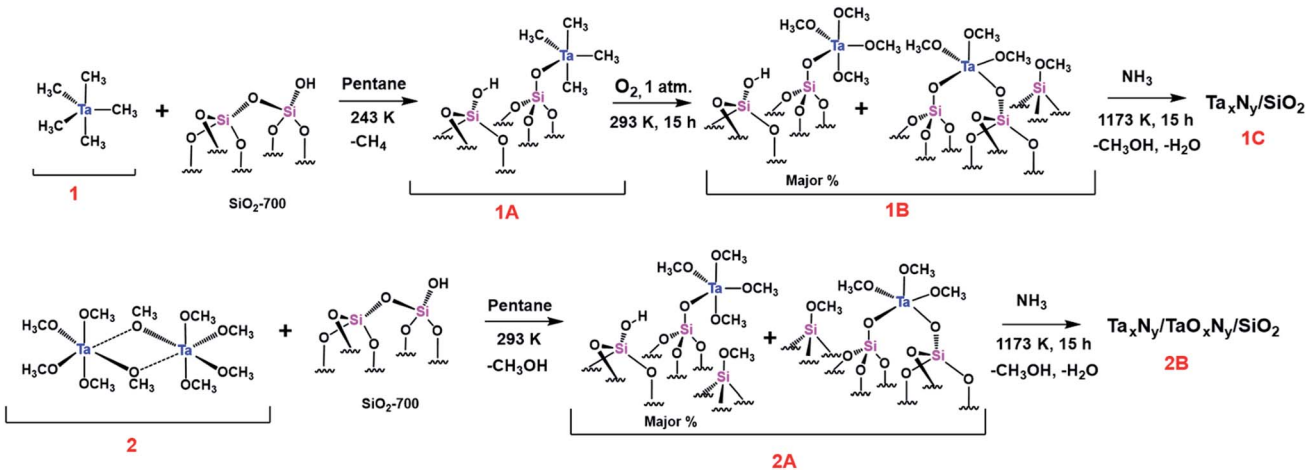


Scheme 1 Two different strategies used for the synthesis of $Ta_xN_y/TaO_xN_y$ NPs (**1C** and **2B** were handled in open air for all the characterizations except for the elemental analysis).

700, resulted in the formation of the supported species **1A** and **2A**, respectively, as shown in Scheme 1. **1A** is formed as predominantly a monopodal species[35–37] that underwent treatment with $O_2$ to form the corresponding tantalum alkoxide **1B** (Scheme 1). A tentative pathway corresponding to the $O_2$ insertion is given in Scheme S1 (in the ESI†).[38,39] **1B** and **2A** are mixtures of monopodal and bipodal species, predominantly the former. A schematic representation of the associated surface reactions that occur during the grafting of **2** is provided in Scheme S2 (ESI†). The precursor **2** exists as a dimer in solution as well as in the solid-state.[40,41] A binuclear-to-mononuclear transition was observed on the silica surface during the grafting, as shown in Scheme S2.† Nitriding of **1B** and **2A** at 1173 K for 15 h resulted in the formation of the corresponding tantalum nitrides/oxynitrides that are depicted as **1C** and **2B**, respectively.

### Characterization of silica-supported tantalum complexes: evidence from IR spectroscopy

IR spectra of $SiO_2$-700, **1A**, **1B**, **2A**, and **2** are given in Fig. 1(A). The spectrum of the support ($SiO_2$-700) alone includes two prominent, well-known vibrations representing the O–H stretching of isolated silanols, at 3746 $cm^{-1}$, and lattice vibrations corresponding to Si–O–Si bridges, at 1985, 1864, and 1635 $cm^{-1}$. The IR spectrum of **1A** includes bands corresponding to the stretching vibrations of C–H bonds ($\nu_{-CH}$) of grafted $Ta(CH_3)_5$ at 2985 and 2932 $cm^{-1}$ ($\nu_{asy}$) and at 2900 and 2855 $cm^{-1}$ ($\nu_{sy}$). Bending vibrations of C–H groups ($\delta_{-CH}$) were observed at approximately 1397 $cm^{-1}$.

Treatment with 1 bar of $O_2$ resulted in the insertion of oxygen atoms into Ta–Me bonds (Scheme S1, ESI†). Corresponding changes in the C–H stretching vibrations are evident in the spectrum of **1B**. Bands corresponding to the C–H stretching vibrations of Ta–O–$CH_3$ at 2960 and 2936 $cm^{-1}$ ($\nu_{asy}$) and 2854 and 2840 $cm^{-1}$ ($\nu_{sy}$) are evident in the spectrum; $\nu_{-CH}$ stretching vibrations corresponding to [(≡Si–O–$CH_3$)] (this notation represents methoxide groups bonded to the silica surface) were observed at 2992 ($\nu_{asy}$) and 2856 $cm^{-1}$ ($\nu_{sy}$).[42,43] Corresponding bending vibrations of C–H in Ta–O–$CH_3$ and ≡Si–O–$CH_3$ were observed at 1454 and 1436 $cm^{-1}$, respectively.

The spectrum of **2A** includes vibrational features similar to those of **1B**, which are assigned to the C–H stretching of Ta–O–$CH_3$ and ≡Si–O–$CH_3$ species. This comparison suggests the presence of similar types of surface species in the samples made from the two precursors. A magnified view of the spectra of **1B**, **2A**, and **2**, Fig. S1 (ESI†), is in line with the suggestion, with the spectrum of **2** supporting the assignments as it shows the stretching and bending vibrations of the precursor complex $Ta(OMe)_5$ at approximately 2919, 2890, and 2823 $cm^{-1}$. However, grafting resulted in ~10–30 $cm^{-1}$ shifts in the vibrational frequencies of Ta–O–$CH_3$ for the complexes **1B** and **2A**.

Because the grafting of **2** was accompanied by the release of methanol, we suggest that it might have opened up a nearby Si–O–Si bridge, resulting in the formation of ≡Si–OH and ≡Si–O–$CH_3$ moieties. Some of the released methanol might also have become adsorbed on the silica. Such adsorbed methanol would likely have been hydrogen bonded with remaining silanols—a possible explanation for the appearance of the broad band in the region of approximately 3400 $cm^{-1}$ in the spectrum of **2A**.

### Silica-supported tantalum complexes: further evidence from elemental analyses

Elemental analysis data presented in Table S2 (ESI†) (samples for elemental analysis were handled under controlled atmospheres) show that the C/Ta value obtained for **1B** is 3.6 ± 0.3, which suggests that the major species formed was monopodal (theoretical C/Ta = 4). **2A** has a C/Ta value of 4.6 ± 0.3, which accounts for the major fraction of monopodal species, with Ta–$(O–CH_3)_4$ formed, along with neighbouring ≡Si–$OCH_3$ groups formed as a result of the reaction of methanol with the strained siloxane bridges (theoretical C/Ta = 5). The elemental analysis data match the expected values for the structures of **1B** and **2A** given in Scheme 1.

### Characterization of supported tantalum nitride NPs

**X-ray diffraction patterns of supported tantalum nitride NPs.** The XRD patterns of **1C** and **2B** include a broad peak corresponding to amorphous silica (Fig. S2, (ESI†)). No peaks representing $Ta_xN_y$/$TaO_xN_y$ are evident, probably a consequence of

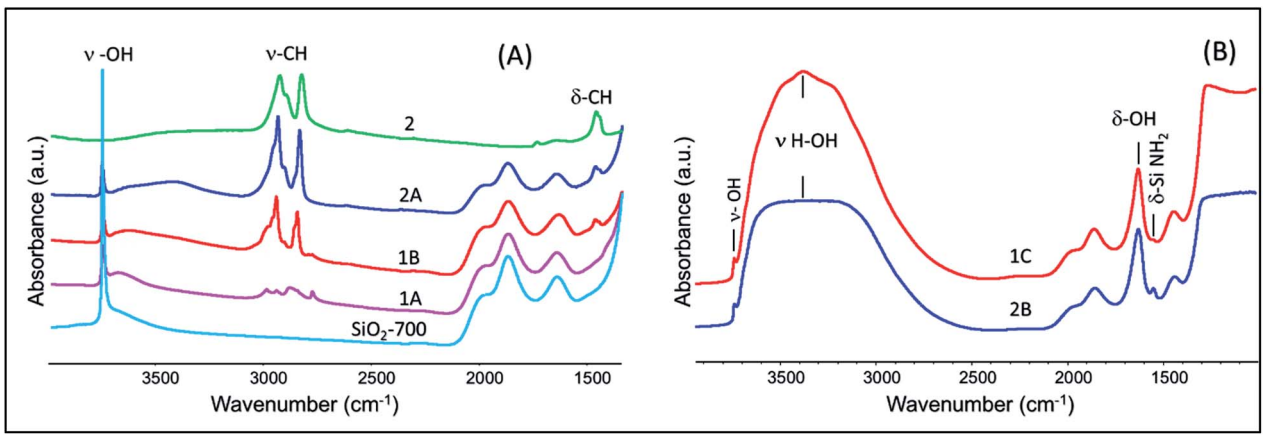


Fig. 1 (A) IR spectra of $SiO_2$-700, **1A**, **1B**, **2A**, and **2**; (B) of **1C** and **2B**.

the too low loading, amorphous nature, and/or the very small size of the particles.[44]

**Transmission electron microscopic analyses of supported tantalum nitride NPs.** In order to understand the size, morphology, and crystalline nature of supported tantalum nitride (**1C** and **2B**), TEM analyses were performed. The images provide evidence that very fine NPs were formed on the silica surface as a result of the nitridation treatment (Fig. 2(A)–(F)). Fig. 2(B) of **1C** shows NPs with diameters in the range between 0.5 and 3 nm. The relatively large particle in the image of Fig. 2(B) is inferred to have formed by coalescence of smaller NPs under the influence of the high-energy electron beam. Fig. 2(B) and (C) show that the NPs are well dispersed on the support surface. Fig. 2(D) is a high-magnification image of **2B** showing the NPs with diameters up to 3.5 nm (Fig. S3, (ESI†)). The slightly greater sizes of the NPs in sample **2B** as compared with **1C** suggest aggregation associated with the greater density of tantalum species in the former sample. Particle size distributions and additional images, determined by HRTEM and STEM, of **1C** and **2B**, are given in Fig. S3–S5 (ESI†). The average particle sizes of **1C** and **2B** samples are respectively 1.6 and 1.9 nm with a standard deviation of ±0.2 nm. These confirm the rather narrow size distribution of the NPs mentioned above, which we suggest may be associated with the preparation strategy. Thus, TEM analysis complements the observations from XRD analysis. Note that some micrographs acquired by HRTEM as shown for **1C** in Fig. 2(A) were sufficient to resolve atomic planes with a *d*-spacing of 0.23 nm, which would possibly match with the {024} plane family of crystalline $Ta_3N_5$ (*Cmcm* (63)).[24]

**IR spectroscopy and elemental analyses of supported tantalum nitride NPs.** IR spectra of **1C** and **2B** (Fig. 1(B)) include a broad band centred at about 3300 $cm^{-1}$ corresponding to adsorbed water and a strong band at 1630 $cm^{-1}$ corresponding to the bending vibrations of adsorbed water. A very weak band assigned to Si–$NH_2$ is also present, at 1550 $cm^{-1}$, in the spectrum of **2B**, and this decreased in intensity upon prolonged exposure of the sample to air.[45] Traces of isolated silanols were also present in both **1C** and **2B** as indicated by the weak band at 3746 $cm^{-1}$. Elemental analysis data presented in Table S2 (ESI†) show that **1C** and **2B** contained 4.2 ± 0.2 and 4.8 ± 0.2 wt% of Ta, respectively.

**Textural properties of support and supported tantalum nitride NPs.** BET surface area measurements were carried out to provide evidence of the textural properties of **1C**, **2B**, and $SiO_2$-700 (Table S3 (ESI†)). Dehydroxylation, grafting of the metal complexes, and subsequent nitriding at 1173 K to form NPs resulted in a reduction of the surface area by 15–20% ($S_{BET}$: 200 $m^2\ g^{-1}$). Nitrogen adsorption–desorption isotherms of the samples **1C**, **2B**, and $SiO_2$-700 are presented in Fig. S6 (ESI†).

**Evidence of tantalum oxidation states of supported NPs.** X-ray photoelectron spectroscopic (XPS) analyses were performed to probe the nature of the surface composition and the oxidation state of Ta. XPS data corresponding to Ta 4f and N 1s of **1C** and **2B** are given in Fig. 3(A)–(D). The Ta 4f spectrum of **1C** shown in Fig. 3(A) is composed of two sets of Ta 4f doublets. As for the doublet in the low energy region, the binding energy values from the Ta 4f spectrum (Ta 4f7/2 = 24.9 eV and Ta 4f5/2 = 26.8 eV) are in good agreement with the Ta 4f of the $Ta_3N_5$ phase (~83%).[46] Another set of doublets observed in the high-energy region (Ta 4f7/2 = 27.7 eV and Ta 4f5/2 = 29.6 eV) most probably should be attributed to the $TaO_xN_y$ phase (~17%). This phase might have arisen from oxidation of the $Ta_3N_5$ that formed. Hence, it is concluded that **1C** (Fig. 3(A)) is predominantly composed of tantalum nitride ($Ta_3N_5$) NPs.[47] In the case of **2B**, the Ta 4f spectrum consists of three separate doublets (Fig. 3(B)) consisting of a weak low energy doublet, similar to the one observed for the TaN phase (Ta 4f7/2 = 23.3 eV and Ta 4f5/2 = 25.2 eV).[48] Another doublet at Ta 4f7/2 = 24.5 eV and Ta 4f5/2 = 26.35 eV and a high-energy doublet at Ta 4f7/2 = 26.5 eV and Ta 4f5/2 = 28.3 eV match well with the $Ta_3N_5$- and TaON-like phases, respectively.[49] The spin orbit splitting constants in all the cases are ~1.9 eV, consistent with the literature.[50]

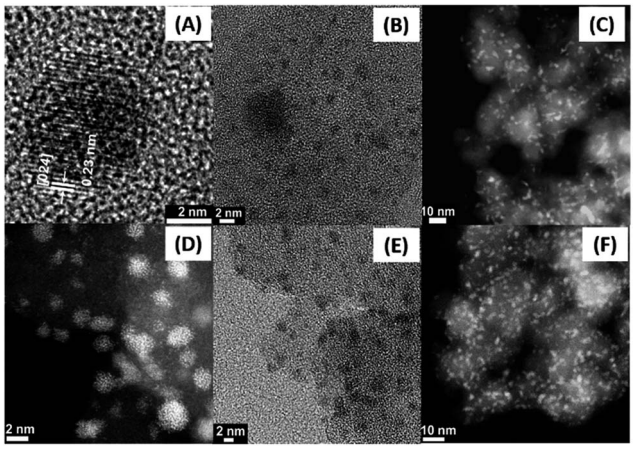


Fig. 2 TEM images of **1C** and **2B**. (A) Lattice-resolved image of one of the particles of **1C**; (B) distribution of $Ta_xN_y$ NPs on silica in **1C**; (C) dark field STEM image showing the dispersion of the NPs in **1C**; (D) high-magnification dark field STEM image of **2B** showing the NPs; (E) NPs in **2B**; and (F) low magnification dark-field STEM image of **2B**.

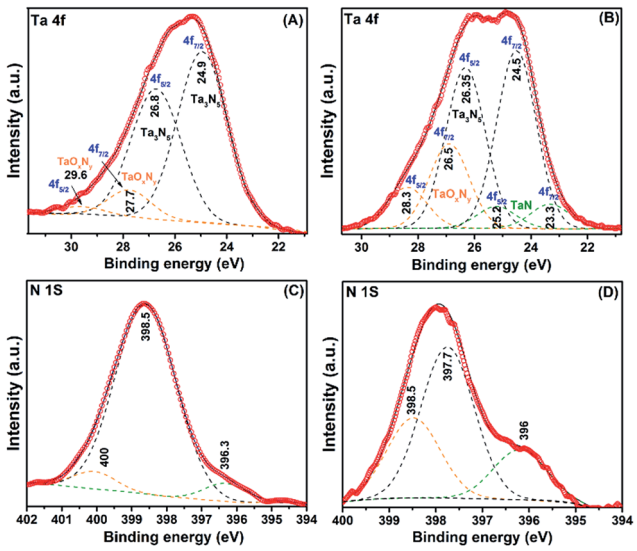


Fig. 3 X-ray photoelectron spectra corresponding to Ta 4f of (A) **1C** (B) **2B** and N 1s of (C) **1C** and (D) **2B**.

XPS data corresponding to the N 1s of **1C** are given in Fig. 3(C). N 1s spectrum shows contributions from three different types of nitrogen environments with their corresponding binding energies at 396.3, 398.5, and 400 eV, similar to the reported values for TaN, $Ta_xN_y$/$Ta_3N_5$, and $TaO_xN_y$ phases, respectively. Slightly different contributions at 396, 397.7, and 398.5 eV were obtained for **2B** as shown in Fig. 3(D).[51,52] For **1C** the main core-level is located at 398.5 eV (~83%) whereas for **2B** the nitrogen core-levels are more evenly distributed among the three binding energies (396, 397.7, and 398.5 eV). The data suggest that the preparation method has a strong impact on the homogeneity of the final synthesized tantalum nitride NPs: starting from the $Ta(Me)_5$ precursor allows one to form the most homogenous tantalum nitride NPs. More spectra (C 1s, O 1s, and Si 2p) are provided for samples **1C** and **2B** in Fig. S7–S9, (ESI†). On the basis of the XPS analyses, we designate samples **1C** and **2B** as a mixture of $Ta_xN_y$ and $TaO_xN_y$ phases.

**UV-visible spectroscopy of supported tantalum nitride NPs.** Fig. 4(A) shows the UV-visible diffuse reflectance spectra of the supported tantalum nitrides **1C** and **2B**. Spectrum (a) shows a red shift of the onset of the absorption at about 636 nm, and the corresponding Tauc plot (Fig. 4(B)b) shows a direct band gap of 2.15 eV. On the other hand, the onset of absorption of the tantalum nitride **2B** is at about 596 nm (Fig. 4(A)b) with a direct band gap of 2.29 eV (Fig. 4(B)b).[53] Bulk $Ta_3N_5$ is characterized by a band gap of 2.1 eV, whereas our as-synthesized $Ta_xN_y$/$TaO_xN_y$ is characterized by band gaps of 2.15 and 2.29 eV for **1C** and **2B**, respectively, indicating a blue shift probably due to the presence of $TaO_xN_y$.[54]

### Details of the molecular surface organotantalum chemistry

A more detailed characterization of the surface species depicted in Scheme 1 required spectroscopic evidence beyond that accessible from the results presented heretofore. NMR and EXAFS spectroscopies provide the further insights summarized in the following paragraphs.

**Evidence from MAS DNP SENS.** Although alkoxides of transition metals have been used extensively as precursors for the preparation of a wide variety of materials, the available crystallographic information characterizing such alkoxides is limited. Correspondingly, there is little such information about precursor **2**. A comparison of the liquid and solid-state NMR spectra of **2** is also missing from the literature. Consequently, we recorded variable-temperature $^1H$ and $^{13}C$ NMR spectra of $Ta(OMe)_5$, **2**, in deuterated dichloromethane, with the results summarized in Fig. S10 and S11 (ESI†), respectively.

The $^1H$ NMR spectrum of dimeric tantalum pentamethoxide **2** in $CD_2Cl_2$ solution at 300 K includes two major resonances, at 4.31 ppm (corresponding to terminal $OCH_3$(a)) and at 4.05 ppm (corresponding to bridging O–C***H***$_3$(c)), and these indicate a rapid intermolecular exchange of terminal and bridging methoxy groups. The low-temperature $^1H$ NMR spectra include three signals with intensity ratios of 2 : 2 : 1, consistent with a dimeric bi-octahedral structure with two bridging methoxy groups. Significantly, the temperature dependence of the spectra indicates that the exchange of terminal methoxide groups occurs faster than the exchange of bridging and terminal methoxide groups.

When the temperature was decreased, the signal at approximately 4.31 ppm split into two distinct singlets, at $\delta$ 4.35 and 4.22 ppm, showing that two types of terminal OC***H***$_3$ groups exist, which are of type (a) and (b), respectively. A weak signal at about 3.33 ppm (C***H***$_3$–OH), corresponding to traces of methanol in the sample, is also evident in the spectra. We surmise that some of the methanol used in the preparation of **2** remained in the samples. A very weak signal at about 5.3 ppm corresponding to trace amounts of C***H***$_2Cl_2$ (from solvent $CD_2Cl_2$) is also evident.

Fig. S11 (ESI†) shows the corresponding $^{13}C$ NMR spectra of **2** at 300 and 193 K. The intensity ratio of terminal carbons to bridging carbons was found to be 2 : 2 : 1, as expected for a dimer. The $^1H$–$^{13}C$ HSQC spectra of $Ta(OMe)_5$ at 193 K (Fig. S12 (ESI†)) show that the signals corresponding to (a) and (b), representing the terminal methoxides, correlate with the carbon signals at 61 and 58 ppm, whereas the bridging methoxide correlates with the carbon signal at 60 ppm. Furthermore, as expected, the $^1H$ signal at 3.33 ppm, attributed to methanol, correlates with the carbon at 50 ppm. The weak $^1H$ signal at 5.3 ppm correlates with the $^{13}C$ signal of ***C***$H_2Cl_2$-$D_2$ (solvent), which appears at 54 ppm.

Fig. 5(A) and (B) is a representation of the solid-state $^{13}C$ CP MAS NMR spectrum of **2** at room temperature and its corresponding two-dimensional $^1H$–$^{13}C$ correlation (HETCOR) spectrum. The $^{13}C$ signals include resonances at 60.4, 58.2, 57.1, and 55.1 ppm, corresponding to a-terminal (a), c-bridging (c), b-terminal (b) methoxides and traces of adsorbed methanol, respectively. Fig. 5(B) confirms these assignments and also indicates the direct correlation with the corresponding protons of various types of methoxides and methanol.

The $^1H$ MAS and $^{13}C$ CP MAS NMR spectra of **1A** show major peaks at 0.8 and 73 ppm, respectively, corresponding to methyl groups of Ta–$CH_3$ (Fig. S13(a) and (b) (ESI†)). The $^{13}C$ CP MAS NMR spectra of **1B** and **2A** (Fig. S14(a) and (b) (ESI†)) show two prominent signals at about 60 and 49 ppm corresponding to Ta–$OCH_3$ and ≡Si–$OCH_3$, respectively (we emphasize that the acquisition time for each of the corresponding spectra was 4–5 days with poor signal-to-noise ratios).

It is thus clear that conventional NMR spectroscopy is limited for characterization of the surface chemistry involved in

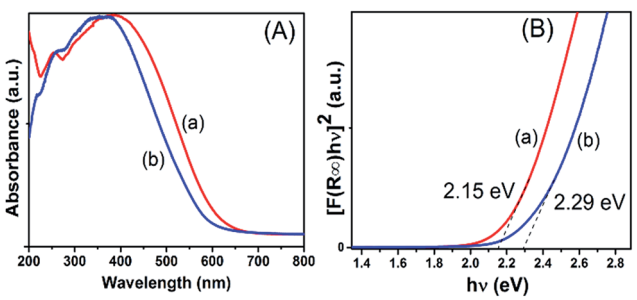


Fig. 4 (A) UV-visible diffuse reflectance spectra of (a) **1C** and (b) **2B**. (B) Tauc plot showing direct band gap of (a) **1C** and (b) **2B**.

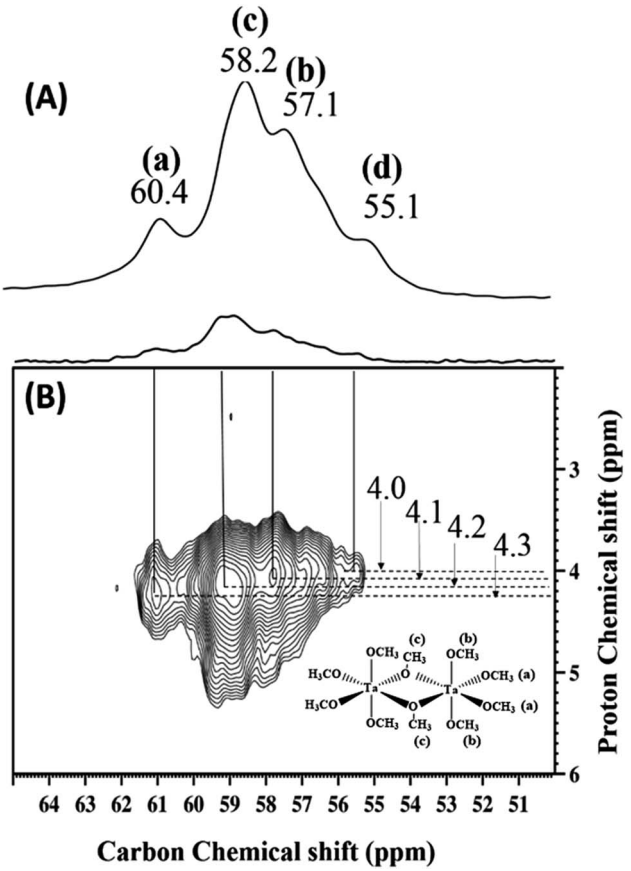


Fig. 5 (A) $^{13}$C CP MAS NMR spectrum of **2** (acquired at 400 MHz, with a 10 kHz MAS frequency, 5000 scans, a 4 s repetition delay, and a 2 ms contact time at room temperature). (B) 2D $^{1}$H–$^{13}$C CP MAS HETCOR spectrum of **2** (acquired at 9.4 T with 10 kHz MAS frequency, 1000 scans per $t_1$ increment, a 4 s repetition delay, 64 individual $t_1$ increments and a 0.2 ms contact time).

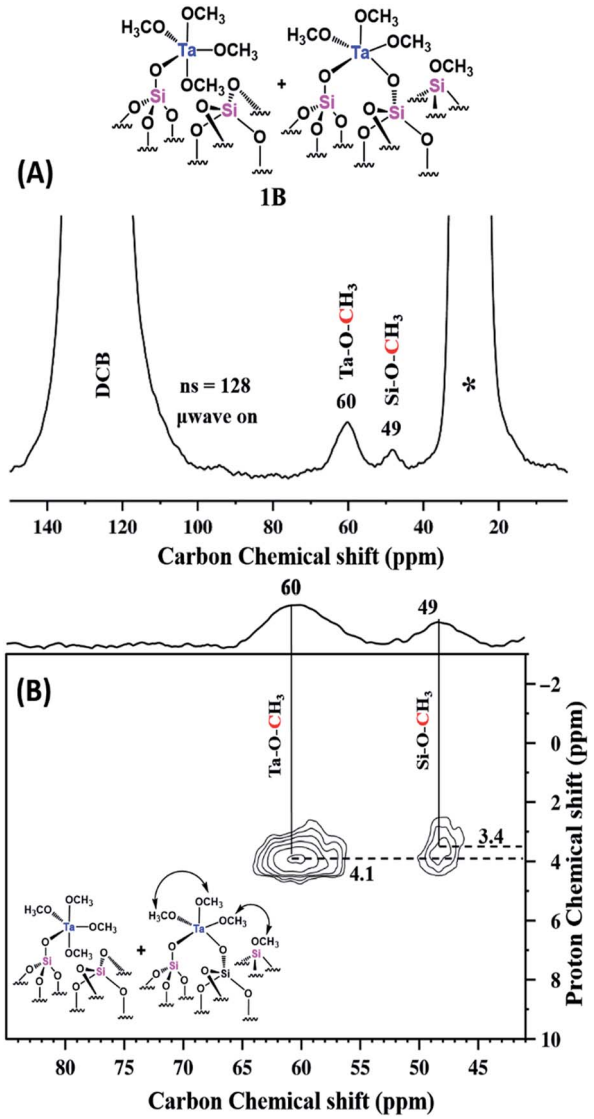


Fig. 6 Schematic representation of **1B** followed by (A) $^{13}$C CP MAS DNP SENS spectra (100 K, 400 MHz/263 GHz gyrotron) of **1B** impregnated with 16 mM of TEKPol in DCB solution. The spectra were recorded using 128 scans, recycle delay of 3 s, contact time of 3 ms, and MAS frequency at 8 kHz. (* indicates the sidebands) (B). Two-dimensional $^{1}$H–$^{13}$C heteronuclear correlation (HETCOR) DNP SENS spectrum of **1B** acquired with 2048 scans per $t_1$ increment, 96 individual increments, and 0.2 ms contact time. During $t_1$, e-DUMBO-1 homonuclear $^{1}$H decoupling was applied and proton chemical shifts were corrected by applying a scaling factor of 0.57 (Table S1 (ESI†)).

the preparation of $Ta_xN_y$ NPs. Hence, we turned to DNP surface-enhanced NMR spectroscopy (SENS) for improved sensitivity. SENS has been used by means of dynamic nuclear polarization (DNP), a technique that allows short acquisition times and is of particular value for samples incorporating species at low concentrations on surfaces.[28] DNP SENS measurements were acquired at about 100 K, with TEKPol (stable radical) as the polarizing agent and 1,1,2,2-tetrachloroethane (TCE) and 1,2-dichlorobenzene (DCB) as the solvents.[55]

The $^{1}$H MAS DNP SENS spectrum of **1B** in TCE (Fig. S15(a) (ESI†)) gave a very good proton enhancement ($\varepsilon_H$) of 112. The $^{13}$C CP MAS DNP SENS spectrum of **1B** shows carbon signals corresponding to the solvent TCE, which overlaps the expected $^{13}$C chemical shifts of Ta–$OCH_3$ and ≡Si–$OCH_3$ (Fig. S15(b) (ESI†)). Hence, another solvent, DCB, was used to disperse the TEKPol, showing a proton enhancement of $\varepsilon_H = 59$ (Fig. S15(c) (ESI†)). The $^{13}$C CP MAS DNP SENS spectrum of **1B** in DCB (Fig. 6(A)) shows the carbon signals corresponding to Ta–O***C***$H_3$ and ≡Si–O***C***$H_3$ at 60 and 49 ppm, respectively, without any interference from the solvent.[56] The spectra were recorded for the sample including $^{13}$C in natural abundance. We were also able to acquire a DNP SENS 2D $^{1}$H–$^{13}$C HETCOR NMR spectrum of **1B** (Fig. 6(B)), which shows correlations of the $^{13}$C signal at 60 ppm with the $^{1}$H signal at 4.1 ppm of Ta–OC***H***$_3$ and the $^{13}$C signal at 49 ppm with the $^{1}$H signal at 3.4 ppm of ≡Si–O–C***H***$_3$.

The MAS DNP SENS spectrum of **2A** in TCE shows a proton and carbon signal enhancement $\varepsilon_H = 147$ and $\varepsilon_C = 62$, respectively (Fig. S16(a) & (b) (ESI†)). Here, for the suppression of TCE solvent signals, we used a CP MAS NMR with echo. The corresponding $^{13}$C CP MAS echo DNP spectrum (Fig. 7(A)) clearly shows two peaks for the sample, at 60 and 49 ppm, corresponding to Ta–O–***C***$H_3$ and ≡Si–O–***C***$H_3$, respectively. As in the case of **1B**, the 2D $^{1}$H–$^{13}$C HETCOR with echo spectrum

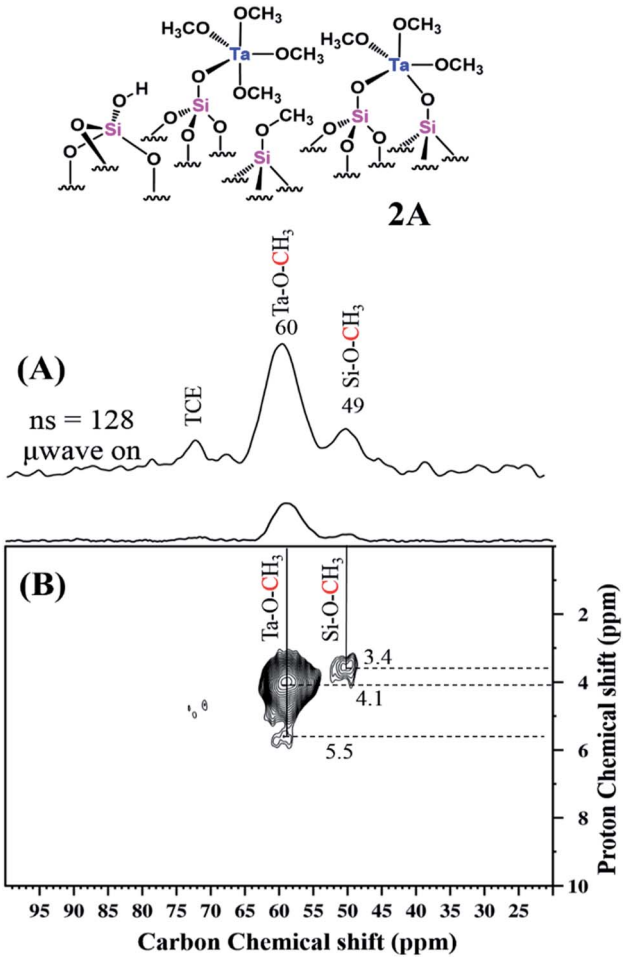


Fig. 7 Schematic representation of **2A** followed by (A) $^{13}C$ CP MAS with echo DNP SENS spectra (100 K, 400 MHz/263 GHz gyrotron) of **2A** impregnated with 16 mM TEKPOL in TCE solution. The spectra were recorded using 128 scans under microwave irradiation, recycle delay of 3 s, contact time of 3 ms, and MAS frequency at 8 kHz (B) 2D $^{1}H$–$^{13}C$ HETCOR DNP SENS spectrum with an echo of **2A** acquired with 2048 scans per $t_1$ increment, 96 individual increments and 0.2 ms contact time. During $t_1$, e-DUMBO-1 homonuclear $^{1}H$ decoupling was applied, and proton chemical shifts were corrected by applying a scaling factor of 0.57 (Table S1 (ESI†)).

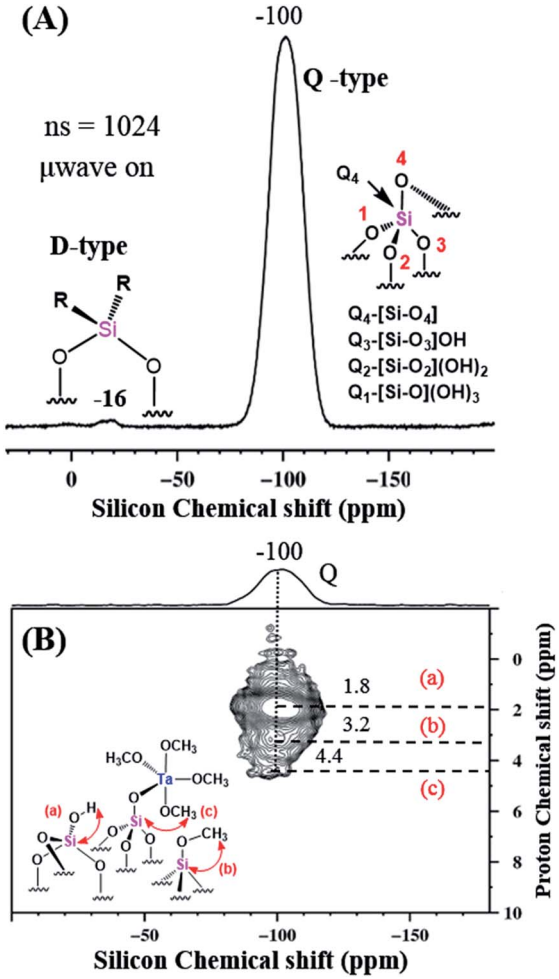


Fig. 8 (A) $^{29}Si$ CP MAS DNP SENS spectra (100 K, 400 MHz/263 GHz gyrotron) of **2A** impregnated with 16 mM TEKPOL in TCE solution. The spectra were recorded with 1024 scans, recycle delay of 3 s, contact time of 5 ms, and MAS frequency at 8 kHz. Separate Q and D type Si species are represented for clarity. (B). 2D $^{1}H$–$^{29}Si$ HETCOR DNP SENS spectrum of **2A** acquired with 2048 scans per $t_1$ increment, 96 individual increments, and 0.2 ms contact time. During $t_1$, e-DUMBO-1 homonuclear $^{1}H$ decoupling was applied, and proton chemical shifts were corrected by applying a scaling factor of 0.57 (Table S1 (ESI†)).

(Fig. 7(B)) of **2A** shows that the $^{13}C$ of $TaOCH_3$ and $\equiv Si–O–CH_3$ correlated with the corresponding $^{1}H$ signals. A weak tail at 60 ppm correlating with the $^{1}H$ at about 5.5 ppm might be evidence of a contribution from the solvent TCE.

The $^{29}Si$ MAS DNP SENS spectrum of **2A** in TCE was acquired with only 1024 scans and showed the presence of Q and D type silicon at −100 and −16 ppm, respectively, attributed to the support Aerosil silica. The nature of the different Q-type Si and the D-type Si signals is explained in Fig. 8(A). The D-type signals are attributed mainly to Si atoms in $(–O–Si(R_2)–O–)_x$ structures (This might be due to the contamination from grease used in the storage tubes). The two-dimensional $^{1}H$–$^{29}Si$ HETCOR DNP-SENS spectrum of **2A**, Fig. 8(B), gives evidence of various Q types correlated with various surroundings of protons, namely, (a) that resulting from the interaction of Q3 with a corresponding OH proton (1.8 ppm); (b) that resulting from the direct interaction of Si of $\equiv Si–OCH_3$ with the corresponding $OCH_3$ proton (3.2 ppm); and (c) that resulting from the Si of ***Si***–O–Ta–O***C****H*$_3$ with the respective proton (4.4 ppm).

$Ta_xN_y/TaO_xN_y$ NPs obtained from both precursors **1B** and **2A** were subjected to DNP SENS analysis. The MAS DNP SENS spectra of **1C** and **2B** in TCE show proton enhancements of 119 and 101, respectively (Fig. S17 (ESI†)). The $^{15}N$ CP MAS DNP SENS spectra of **1C** and **2B** were recorded with only 3072 scans (Fig. 9). In the case of **1C**, the spectrum shows an intense signal at about 24 ppm that is attributed to $Ta_xN_y$ (Fig. 9(A)). For **2B**, in addition to the peak at 24 ppm, a signal at 10 ppm is clearly visible that can be assigned to $TaO_xN_y$ (Fig. 9(C)). There is only one report that describes a similar type of NMR observation for such small clusters of tantalum nitride;[57] Wolczansky *et al.* demonstrated that similar types of alkylidene precursors generated clusters/oligomers of amorphous tantalum nitride at

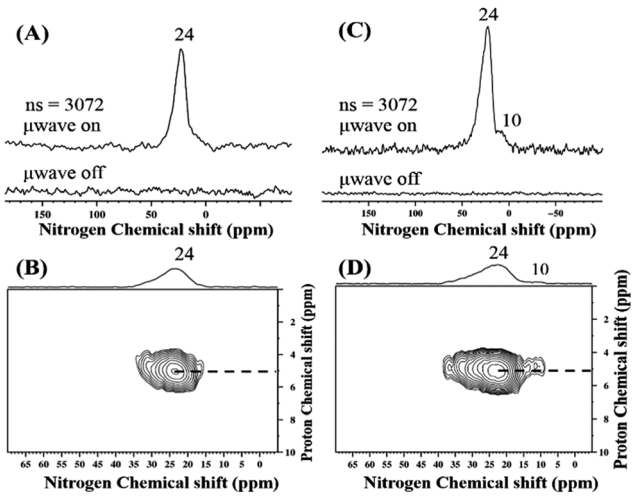


Fig. 9 $^{15}N$ CP MAS DNP SENS spectrum (100 K, 400 MHz/263 GHz gyrotron) of (A) **1C** and (C) **2B** impregnated with 16 mM TEKPol in TCE solution. The spectra were recorded with 3072 scans under microwave irradiation, recycle delay of 3 s, contact time of 4 ms, and MAS frequency at 8 kHz. (B) and (D) Two-dimensional $^{1}H-^{15}N$ HETCOR DNP SENS spectrum of **1C** and **2B** acquired with 2048 scans per $t_1$ increment, 96 individual increments, and 4 ms contact time. During $t_1$, e-DUMBO-1 homonuclear $^{1}H$ decoupling was applied, and proton chemical shifts were corrected by applying a scaling factor of 0.57. See Table S1† for the details.

Table 1 Summary of results of XAS characterizing $SiO_2$-700-supported Ta complexes[a]

| Sample | Shell | $N$ | $R$ (Å) | $\Delta\sigma^2 \times 10^3$ (Å$^2$) | $\Delta E_0$ (eV) |
|---|---|---|---|---|---|
| **1A** | Ta–$C_m$ | 4.0 | 2.20 | 3.0 | −10.0 |
| | Ta–$O_s$ | 1.5 | 1.90 | 1.0 | −9.7 |
| **1B** Model I | Ta–$O_{mo/s}$ | 2.0 | 1.86 | 3.7 | 3.2 |
| | Ta–C | 2.3 | 2.57 | 1.1 | 14.4 |
| | Ta–$C_{mo}$ | 3.5 | 3.18 | 6.2 | −14.7 |
| | Ta–$O_l$ | 5.2 | 3.76 | 10.4 | −6.6 |
| **1B** Model II | Ta–$O_{mo/s}$ | 2.0 | 1.85 | 3.6 | 4.6 |
| | Ta–O | 1.6 | 2.55 | 1.4 | 7.5 |
| | Ta–$C_{mo}$ | 4.2 | 3.20 | 8.2 | −14.7 |
| | Ta–$O_l$ | 3.7 | 3.75 | 6.4 | −5.8 |
| **2** | Ta–$O_{t\text{-}mo}$ | 2.0 | 1.88 | 4.7 | 3.8 |
| | Ta–$O_{b\text{-}mo}$ | 2.0 | 2.20 | 3.4 | −2.7 |
| | Ta–$C_{mo}$ | 4.0 | 3.15 | 9.9 | −13.6 |
| | Ta–Ta | 1.2 | 3.40 | 4.5 | −11.2 |
| **2A** | Ta–$O_{mo/s}$ | 3.3 | 1.88 | 6.3 | 1.5 |
| | Ta–$C_{mo}$ | 3.3 | 3.11 | 0.1 | −16.6 |
| | Ta–$Si_s$ | 2.8 | 3.33 | 5.2 | 3.7 |
| | Ta–$O_l$ | 5.8 | 3.78 | 10.9 | −8.3 |

[a] Notation: $N$, coordination number; $R$, absorber-backscatterer distance; $\Delta\sigma^2$, disorder term (Debye–Waller factor); $\Delta E_0$, inner potential correction; m, methyl; s, support; mo, methoxy; l, long; t-mo, terminal methoxy; b-mo, bridging methoxy. Estimated error bounds for each parameter are as follows: $N \pm 20\%$; $R \pm 0.02$ Å; $\Delta\sigma^2 \pm 20\%$; $\Delta E_0 \pm 20\%$.

temperatures below 673 K and crystalline cubic tantalum nitride at temperatures above 1023 K. They also observed that the $^{15}N$ signal corresponding to $Ta_xN_y$ shifted upfield in the case of small partially amorphous clusters.

In general, the $^{15}N$ signal for a bulk transition metal nitride is expected as a broad band at ~400 ppm.[58] For NPs of metal nitrides, the corresponding signal is shifted up field to 24 ppm (Fig. 9(A)). Moreover, as the coordinating nitrogen is replaced by oxygen, the $^{15}N$ signal corresponding to $TaO_xN_y$ is further shifted to 10 ppm (Fig. 9(C)). The $^{1}H-^{15}N$ HETCOR DNP SENS spectra of **1C** and **2B** (Fig. 9(B) & (D)) recorded with the long contact time of 5 ms show a distant correlation with the $^{1}H$ of the solvent, which appears at about 5 ppm. Thus, the $^{15}N$ DNP SENS results complement the XPS results.

**Evidence from EXAFS spectroscopy.** X-ray absorption spectroscopy (XAS) provides detailed information about the local electronic and geometric structure of an absorber atom and its near surroundings. XAS experiments characterizing $SiO_2$-700-supported tantalum complexes, namely, **1A**, **1B**, **2**, and **2A** were carried out at the Ta $L_{III}$ edge (9881 eV), in a specially designed cell with the samples at liquid nitrogen temperature, under high vacuum to prevent exposure to air or moisture.[59]

EXAFS data analysis was carried out with the software packages ATHENA and XDAP.[60,61] Reference files used for phase shift and backscattering amplitude corrections were calculated with the FEFF 7.0 code.[62] A summary of the results is presented in Table 1, and the details of the fitting and analyses are presented in Fig. S18–S30 and Tables S6–S9 (ESI†).

The best-fit model for **1A** is consistent with the expectation of methyl groups and support oxygen atoms bonded to the tantalum. The model thus gives evidence of a Ta–C contribution and a Ta–O contribution. The non-integer Ta–O coordination number (Table 1) could be an indication of the presence of some bipodal species, possibly formed under the influence of the X-ray beam during the measurement, as was observed for a silica-supported tungsten complex.[63] The results are nonetheless consistent with the expectation that the sample consisted of predominantly of monopodal species, [(≡SiO–)$Ta(CH_3)_4$].

In fitting the data characterizing sample **1B**, two different models were considered to resolve O in the support and O in the methoxy groups. They are Models I and II, consisting of four shells, the maximum number justified by the data: (1) a Ta–O contribution (where O represents unresolved methoxy and support O atoms), (2) a Ta–C contribution, (3) another Ta–O contribution to represent the interaction of Ta with O atoms of the support at a distance greater than a bonding distance, and (4) another Ta-light atom contribution. In Model I, the light atom is C; in Model II, it is O. These models provided satisfactory fits of the data, with Model II giving a slightly better fit than the other. The important point is the confirmation of the presence of methoxy groups on the Ta, with Ta–O and a Ta–C contributions at appropriate distances for tantalum methoxy species (Table 1). But the results are less than quantitative, failing to resolve all of the Ta–C and Ta–O contributions, and thus reflecting the limitations of EXAFS spectroscopy for structures such as ours.

EXAFS spectroscopy was also used to characterize the dimeric precursor **2**, for which there is no known crystal

structure. The results (Table 1) demonstrate a Ta–Ta contribution, with a coordination number of 1 (within error) at a distance of 3.34 Å, consistent with a dimer. The EXAFS data also give evidence of methoxy groups (Table 1), but the C/Ta and O/Ta ratio suggested from the Ta–O and Ta–C coordination numbers is about 3, rather than the value of 5 expected for $Ta(OMe)_5$. Thus, the data are less than sufficient for a structure determination, and we postulate that the sample was degraded under the influence of the X-ray beam in the experiment, consistent with our observation that the second and third scans were different from the first (the third scan was used in the data analysis, because the data quality was higher than that of the earlier scans).

An approach similar to that described above for sample **1B** was used in fitting the data characterizing the supported sample prepared from precursor **2**, that is, **2A**. Again, it was found that resolution of the various Ta–O contributions was not justified by the data, and so a simplified model was used (Table 1). The best-fit model leads to the important result that there is no EXAFS evidence of a Ta–Ta contribution, and thus there is support for the above-stated inference that the dimers broke and gave single-site species.

Thus, although EXAFS data were not sufficient to provide conclusive evidence of the exact structures of **1B** and **2**, the best-fit models support the following hypothesis: (a) transformation of **1** to **1B** takes place by oxygen insertion (Ta–C to Ta–O–C), (b) **2** is a dimer with two bridging methoxide ligands with a Ta–Ta contribution, (c) **2A** is a single-site species with no Ta–Ta contribution, and (d) **1B** and **2A** are similar types of surface species.

### Catalytic properties of silica-supported tantalum nitride NPs

$Ta_xN_y$ and $TaO_xN_y$ NPs (**1C** and **2B**) were tested as catalysts for cyclooctene epoxidation with liquid-phase reactants including 30 wt% $H_2O_2$ as the oxidant. Dilute hydrogen peroxide is one of the most convenient oxidants for epoxide formation because of its ease of handling and high oxygen content, and the relative lack of by-products in the reactions.[64,65] The reaction conditions were as follows: a volume of 0.92 mL of cyclooctene in 4 mL of methanol with 4–70 mg of catalyst was used in a batch reactor; 3 mL of $H_2O_2$ was used as the oxidant. The epoxidation reaction was carried out at 333 K for 18 h under refluxing conditions. Blank experiments were conducted in the absence of either a catalyst or $H_2O_2$ to assess the activity. No conversion was observed in the absence of the peroxide. In contrast, 8% conversion and approximately 98% selectivity were observed in the presence of $H_2O_2$ but in the absence of a catalyst. The catalyst performance data are presented in Fig. 10 and Table S4(a) (ESI†).

Turnover numbers as high as 1395 were observed with 0.2 wt% of Ta in the catalyst. With an increase in Ta content, a gradual decrease of TON values was observed.[66] In contrast, conversion increased with increasing catalyst Ta content. The product formed was mainly cyclooctene epoxide with traces of cyclooctene diol. The observed selectivities were between 98 and 99% for the lower catalyst Ta loadings. A reaction with Aerosil

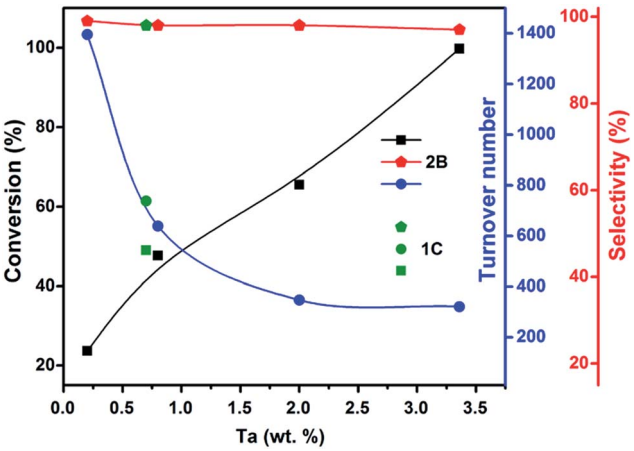


Fig. 10 Catalytic activities of **2B** and **1C** for cyclooctene epoxidation. (Black-conversion; blue-TON; red-selectivity) [reaction conditions: 0.92 mL of cyclooctene; 4–70 mg of catalyst; 4 mL of methanol and 3 mL of $H_2O_2$ (30 wt%); @ 333 K for 18 h].

silica but without NPs was conducted to provide evidence of the effect of the support. Results were similar to that of the blank reaction (performed with $H_2O_2$ but no catalyst) showing a conversion of ~10% and a relatively low selectivity of ~87%. Thus, silica is not just an innocent spectator in this partial oxidation reaction, but its effect under our reaction conditions was minimal, corresponding to its weak Brønsted acidity.[67] The catalyst performance data indicate that **1C** (Ta content ~0.7 wt%) shows only slightly better performance than **2B**, which might be attributed to the smaller particles of **1C**. For Ta contents below 3.4 wt%, the observed selectivities were ~98%. Yet, similar selectivities were observed for various Ta contents. However, a further increase in Ta content resulted in a decline in the selectivity. A significant improvement in the conversion, from 23 to 99% or more, was achievable with increasing Ta content.

On the basis of reported[17] mechanisms, we suggest that only surface Ta sites, which are either oxo or bis-hydroxide, could be the active sites (Scheme S3 (ESI†)). Because the surface to volume ratio of the NPs is high, they have more Ta sites than the corresponding masses of bulk tantalum nitrides and are evidently more efficient catalysts. Gao *et al.*[17] reported that pure $Ta_3N_5$ has a higher basicity than TaON. High basicity might induce the decomposition of $H_2O_2$. As a result, the effective amount of $H_2O_2$ available in the reaction medium may not be sufficient for the formation of tantalum hydroperoxide active sites. Their study has shown that TaON with controlled basicity influences the epoxidation activity positively. The surface of tantalum nitride NPs undergoes oxidation to form a similar surface layer of $TaO_xN_y$ which probably generates the active sites during the reaction, and this might be the reason for the observed similarities in activities of **1C** and **2B**. XPS results show the presence of $TaO_xN_y$ phase in **1C**.

Gao *et al.*[17] used unsupported $Ta_3N_5$/TaON NPs (~20 nm in average diameter) for the same reaction. They found approximately 57% conversion with $Ta_2O_5$, whereas $Ta_3N_5$ or TaON showed higher conversions, including, for example, 97%

 

conversion with 96% selectivity with TaON nanoclusters being the best. By making use of supported NPs (0.5–3 nm in diameter) for the same reaction under similar reaction conditions, we observed conversions approaching 100% without loss of selectivity with a catalyst Ta content as low as ~3.4 wt%. Notably, we did not observe any leaching of the active species from the surface. The substrate scope of the $Ta_xN_y$ supported catalyst was probed with other substrates such as styrene, cyclohexene, and 1-octene and the results are presented in Table S4(b) (ESI†).

We compared the observed activities with literature values (shown for catalysts incorporating transition metals and supported on silica) for the catalytic cyclooctene epoxidation (Table S4(a) and S5 (ESI†)). Although a direct comparison of our data with literature data is not possible, we have sufficient data to infer that the activities reported in the literature are lower than that of the supported nitride/oxynitride catalyst reported here. At all of the Ta loadings tested, high selectivities were obtained for cyclooctene epoxide, both with samples **1C** and **2B**. These observations and the comparisons with the literature suggest that our metal nitride or metal oxynitride/silica samples could be promising alternatives to metal/silica catalysts for the cyclooctene epoxidation reaction. On the basis of the literature, we suggest a tentative mechanism for the cyclooctene epoxidation catalyzed by $Ta_xN_y/TaO_xN_y$ NPs on silica, as summarized in Scheme S3.†[17,68–73]

## Conclusions

Highly dispersed $Ta_xN_y/TaO_xN_y$ NPs with diameters in the range of 0.5 to 3 nm supported on silica were synthesized from supported tantalum complexes according to the strategy of surface organometallic chemistry. Characterization of the surface species at various stages of the synthesis by a range of spectroscopic and microscopic methods gave evidence of the chemistry. Especially helpful was solid-state NMR spectroscopy, specifically, DNP SENS, for understanding this chemistry—this technique enabled the sensitive detection of hetero nuclei including $^{13}C$, $^{15}N$, and $^{29}Si$ with the aid of the polarizing agent TEKPol. The results indicate oxygen insertion into supported tantalum alkyl complexes to form tantalum alkoxides at room temperature. NMR and EXAFS data provide evidence of a binuclear to mononuclear transformation of $Ta_2(OMe)_{10}$ upon grafting to the support. Irrespective of whether the precursor was mono- or binuclear, nitriding resulted in the formation of a mixture of $Ta_xN_y$ and $TaO_xN_y$ NPs from the molecular precursors, with the sizes depending on the precursor. The NPs catalyse cyclooctene epoxidation with selectivities of ~98% at conversions of ~99%.

## Acknowledgements

We gratefully acknowledge the financial support provided by the King Abdullah University of Science and Technology (KAUST). We thank Dr Kun Li, Dr Nejib Hedili, and Dr Abdul-Hamid Emwas of the KAUST core labs for HRTEM, XPS, and NMR measurements, respectively, and Prof. Kazuhiro Takanabe for help with the ammonia treatments. We acknowledge Prof. Lyndon Emsley, EPFL, Switzerland, for helpful suggestions. We acknowledge beam time at beamline 4-1 of the Stanford Synchrotron Radiation Lightsource supported by the U.S. DOE Division of Materials Science under Contract No. DE-AC02-76SF00515.

## Notes and references

1 A. Borodziński and M. Bonarowska, *Langmuir*, 1997, **13**, 5613–5620.
2 W. Lu and C. M. Lieber, *Nat. Mater.*, 2007, **6**, 841–850.
3 J. Yang, T. Ling, W.-T. Wu, H. Liu, M.-R. Gao, C. Ling, L. Li and X.-W. Du, *Nat. Commun.*, 2013, **4**, 1695.
4 (*a*) X. Cheng, S. B. Lowe, P. J. Reece and J. J. Gooding, *Chem. Soc. Rev.*, 2014, **43**, 2680–2700; (*b*) C.-T. Ho, K.-B. Low, R. F. Klie, K. Maeda, K. Domen, R. J. Meyer and P. T. Snee, *J. Phys. Chem. C*, 2011, **115**, 647–652.
5 L. Fan, M. Zhu, X. Lee, R. Zhang, K. Wang, J. Wei, M. Zhong, D. Wu and H. Zhu, *Part. Part. Syst. Charact.*, 2013, **30**, 764–769.
6 C. Zhen, L. Wang, G. Liu, G. Q. Lu and H.-M. Cheng, *Chem. Commun.*, 2013, **49**, 3019–3021.
7 T. Hisatomi, M. Otani, K. Nakajima, K. Teramura, Y. Kako, D. Lu, T. Takata, J. N. Kondo and K. Domen, *Chem. Mater.*, 2010, **22**, 3854–3861.
8 G. H. Carey, A. L. Abdelhady, Z. Ning, S. M. Thon, O. M. Bakr and E. H. Sargent, *Chem. Rev.*, 2015, **115**, 12732–12763.
9 J. P. Wilcoxon, T. Martino, E. Klavetter and A. P. Sylwester, in *Nanophase Materials: Synthesis—Properties—Applications*, ed. G. C. Hadjipanayis and R. W. Siegel, Springer Netherlands, Dordrecht, 1994, pp. 771–780, DOI: 10.1007/978-94-011-1076-1_80.
10 T. Bligaard, R. M. Bullock, C. T. Campbell, J. G. Chen, B. C. Gates, R. J. Gorte, C. W. Jones, W. D. Jones, J. R. Kitchin and S. L. Scott, *ACS Catal.*, 2016, **6**, 2590–2602.
11 F. Humblot, J. P. Candy, F. Le Peltier, B. Didillon and J.-M. Basset, *J. Catal.*, 1998, **179**, 459–468.
12 H. Zhu, D. H. Anjum, Q. Wang, E. Abou-Hamad, L. Emsley, H. Dong, P. Laveille, L. Li, A. K. Samal and J.-M. Basset, *J. Catal.*, 2014, **320**, 52–62.
13 C. R. Kagan and C. B. Murray, *Nat. Nanotechnol.*, 2015, **10**, 1013–1026.
14 A. P. Alivisatos, *Science*, 1996, **271**, 933–937.
15 W. Jiang, C. Siming, S. Alwyn and L. Huiyun, *J. Phys. D: Appl. Phys.*, 2015, **48**, 363001.
16 X. Wang, G. Sun, N. Li and P. Chen, *Chem. Soc. Rev.*, 2016, **45**, 2239–2262.
17 Q. S. Gao, S. N. Wang, Y. C. Ma, Y. Tang, C. Giordano and M. Antonietti, *Angew. Chem., Int. Ed.*, 2012, **51**, 961–965.
18 Q. S. Gao, C. Giordano and M. Antonietti, *Small*, 2011, **7**, 3334–3340.
19 Q. Gao, C. Giordano and M. Antonietti, *Angew. Chem.*, 2012, **124**, 11910–11914.
20 Q. Gao, C. Giordano and M. Antonietti, *Small*, 2011, **7**, 3334–3340.

21 Z. Wang, J. Hou, S. Jiao, K. Huang and H. Zhu, *J. Mater. Chem.*, 2012, **22**, 21972–21978.
22 K. Maeda, *ACS Catal.*, 2013, **3**, 1486–1503.
23 Y. Sasaki, Z. Tokuyasu, Y. Ono, M. Iwasaki and S. Ito, *Adv. Mater. Sci. Eng.*, 2009, **2009**, 4.
24 Y.-C. Wang, C.-Y. Chang, T.-F. Yeh, Y.-L. Lee and H. Teng, *J. Mater. Chem. A*, 2014, **2**, 20570–20577.
25 M. Jansen and H. P. Letschert, *Nature*, 2000, **404**, 980–982.
26 (*a*) A. J. Rossini, A. Zagdoun, M. Lelli, A. Lesage, C. Copéret and L. Emsley, *Acc. Chem. Res.*, 2013, **46**, 1942–1951; (*b*) E. Pump, J. Viger-Gravel, E. Abou-Hamad, M. K. Samantaray, B. Hamzaoui, A. Gurinov, D. H. Anjum, D. Gajan, A. Lesage, A. Bendjeriou-Sedjerari, L. Emsley and J.-M. Basset, *Chem. Sci.*, 2017, **8**, 284–290.
27 L. Piveteau, T.-C. Ong, A. J. Rossini, L. Emsley, C. Copéret and M. V. Kovalenko, *J. Am. Chem. Soc.*, 2015, **137**, 13964–13971.
28 E. Bouleau, P. Saint-Bonnet, F. Mentink-Vigier, H. Takahashi, J. F. Jacquot, M. Bardet, F. Aussenac, A. Purea, F. Engelke, S. Hediger, D. Lee and G. De Paepe, *Chem. Sci.*, 2015, **6**, 6806–6812.
29 A. Lesage, M. Lelli, D. Gajan, M. A. Caporini, V. Vitzthum, P. Miéville, J. Alauzun, A. Roussey, C. Thieuleux, A. Mehdi, G. Bodenhausen, C. Coperet and L. Emsley, *J. Am. Chem. Soc.*, 2010, **132**, 15459–15461.
30 M. Valla, A. J. Rossini, M. Caillot, C. Chizallet, P. Raybaud, M. Digne, A. Chaumonnot, A. Lesage, L. Emsley, J. A. van Bokhoven and C. Copéret, *J. Am. Chem. Soc.*, 2015, **137**, 10710–10719.
31 O. A. Nikonova, G. A. Seisenbaeva, V. G. Kessler, P. A. Shcheglov and D. V. Drobot, *Russ. J. Inorg. Chem.*, 2007, **52**, 1687–1693.
32 C. Copéret, A. Comas-Vives, M. P. Conley, D. P. Estes, A. Fedorov, V. Mougel, H. Nagae, F. Núñez-Zarur and P. A. Zhizhko, *Chem. Rev.*, 2016, **116**, 323–421.
33 A. Johansson, M. Roman, G. A. Seisenbaeva, L. Kloo, Z. Szabo and V. G. Kessler, *J. Chem. Soc., Dalton Trans.*, 2000, 387–394, DOI: 10.1039/A907720K.
34 M. T. Vandenborre, B. Poumellec, C. Alquier and J. Livage, *J. Non-Cryst. Solids*, 1989, **108**, 333–337.
35 Y. Chen, E. Abou-hamad, A. Hamieh, B. Hamzaoui, L. Emsley and J.-M. Basset, *J. Am. Chem. Soc.*, 2015, **137**, 588–591.
36 Y. Chen, S. Ould-Chikh, E. Abou-Hamad, E. Callens, J. C. Mohandas, S. Khalid and J.-M. Basset, *Organometallics*, 2014, **33**, 1205–1211.
37 R. R. Schrock and P. Meakin, *J. Am. Chem. Soc.*, 1974, **96**, 5288–5290.
38 E. C. Garrett, T. M. Figg and T. R. Cundari, *Inorg. Chem.*, 2014, **53**, 7789–7798.
39 S.-J. Chen and Z.-L. Xue, *Organometallics*, 2010, **29**, 5579–5584.
40 L. G. Hubert-Pfalzgraf and J. G. Riess, *Inorg. Chem.*, 1975, **14**, 2854–2856.
41 D. C. Bradley and C. E. Holloway, *J. Chem. Soc. A*, 1968, 219–223.
42 R. P. Saint-Arroman, J.-M. Basset, F. Lefebvre and B. Didillon, *Appl. Catal., A*, 2005, **290**, 181–190.
43 L. J. Burcham, G. Deo, X. Gao and I. E. Wachs, *Top. Catal.*, 2000, **11**, 85–100.
44 (*a*) Y. Luo, J. Yi, D. Tong and C. Hu, *Green Chem.*, 2016, **18**, 848–857; (*b*) R. K. Singha, S. Ghosh, S. S. Acharyya, A. Yadav, A. Shukla, T. Sasaki, A. M. Venezia, C. Pendem and R. Bal, *Catal. Sci. Technol.*, 2016, **6**, 4601–4615.
45 A. Noshay, M. Matzner and T. C. Williams, *Ind. Eng. Chem. Prod. Res. Dev.*, 1973, **12**, 268–277.
46 E. Nurlaela, S. Ould-Chikh, M. Harb, S. del Gobbo, M. Aouine, E. Puzenat, P. Sautet, K. Domen, J.-M. Basset and K. Takanabe, *Chem. Mater.*, 2014, **26**, 4812–4825.
47 L. Li, E.-W. Niu, G.-H. Lv, W.-R. Feng, W.-C. Gu, G.-L. Chen, G.-L. Zhang, S.-H. Fan, C.-Z. Liu and S.-Z. Yang, *Chin. Phys. Lett.*, 2006, **23**, 3018.
48 N. Arshi, J. Lu, Y. K. Joo, J. H. Yoon and B. H. Koo, *Surf. Interface Anal.*, 2015, **47**, 154–160.
49 H. X. Dang, N. T. Hahn, H. S. Park, A. J. Bard and C. B. Mullins, *J. Phys. Chem. C*, 2012, **116**, 19225–19232.
50 A. Arranz and C. Palacio, *Appl. Phys. A*, 2005, **81**, 1405–1410.
51 M. Chisaka, A. Ishihara, N. Uehara, M. Matsumoto, H. Imai and K. Ota, *J. Mater. Chem. A*, 2015, **3**, 16414–16418.
52 M. Liao, J. Feng, W. Luo, Z. Wang, J. Zhang, Z. Li, T. Yu and Z. Zou, *Adv. Funct. Mater.*, 2012, **22**, 3066–3074.
53 Y. Kado, C.-Y. Lee, K. Lee, J. Muller, M. Moll, E. Spiecker and P. Schmuki, *Chem. Commun.*, 2012, **48**, 8685–8687.
54 E. Nurlaela, M. Harb, S. del Gobbo, M. Vashishta and K. Takanabe, *J. Solid State Chem.*, 2015, **229**, 219–227.
55 A. Zagdoun, G. Casano, O. Ouari, M. Schwarzwälder, A. J. Rossini, F. Aussenac, M. Yulikov, G. Jeschke, C. Copéret, A. Lesage, P. Tordo and L. Emsley, *J. Am. Chem. Soc.*, 2013, **135**, 12790–12797.
56 M. W. McKittrick and C. W. Jones, *Chem. Mater.*, 2003, **15**, 1132–1139.
57 M. M. Banaszak Holl, P. T. Wolczanski, D. Proserpio, A. Bielecki and D. B. Zax, *Chem. Mater.*, 1996, **8**, 2468–2480.
58 K. J. D. MacKenzie, R. H. Meinhold, D. G. McGavin, J. A. Ripmeester and I. Moudrakovski, *Solid State Nucl. Magn. Reson.*, 1995, **4**, 193–201.
59 R. E. Jentoft, S. E. Deutsch and B. C. Gates, *Rev. Sci. Instrum.*, 1996, **67**, 2111–2112.
60 E. A. Stern, M. Newville, B. Ravel, Y. Yacoby and D. Haskel, *Phys. B*, 1995, **208**, 117–120.
61 M. Newville, *J. Synchrotron Radiat.*, 2001, **8**, 96–100.
62 S. I. Zabinsky, J. J. Rehr, A. Ankudinov, R. C. Albers and M. J. Eller, *Phys. Rev. B: Condens. Matter Mater. Phys.*, 1995, **52**, 2995–3009.
63 N. Maity, S. Barman, E. Callens, M. K. Samantaray, E. Abou-Hamad, Y. Minenkov, V. D'Elia, A. S. Hoffman, C. M. Widdifield, L. Cavallo, B. C. Gates and J.-M. Basset, *Chem. Sci.*, 2016, **7**, 1558–1568.
64 W. R. Sanderson, *Pure Appl. Chem.*, 2000, **72**, 1289–1304.
65 R. Noyori, M. Aoki and K. Sato, *Chem. Commun.*, 2003, 1977–1986, DOI: 10.1039/B303160H.
66 S. Xue, G. Chen, Z. Long, Y. Zhou and J. Wang, *RSC Adv.*, 2015, **5**, 19306–19314.

67 P. Chandra, D. S. Doke, S. B. Umbarkar, K. Vanka and A. V. Biradar, *RSC Adv.*, 2015, **5**, 21125–21131.
68 P. J. Cordeiro and T. D. Tilley, *ACS Catal.*, 2011, **1**, 455–467.
69 D. A. Ruddy and T. D. Tilley, *Chem. Commun.*, 2007, 3350–3352.
70 N. Morlanes and J. M. Notestein, *Appl. Catal., A*, 2010, **387**, 45–54.
71 U. Arnold, R. Serpa da Cruz, D. Mandelli and U. Schuchardt, *J. Mol. Catal. A: Chem.*, 2001, **165**, 149–158.
72 N. A. Stephenson and A. T. Bell, *J. Am. Chem. Soc.*, 2005, **127**, 8635–8643.
73 M.-L. Lin, K. Hara, Y. Okubo, M. Yanagi, H. Nambu and A. Fukuoka, *Catal. Commun.*, 2011, **12**, 1228–1230.